Article

Journal of
Nanoscience and Nanotechnology
Vol. 20, 1–8, 2020
www.aspbs.com/jnn

Enhancing Photocatalytic Activity of Nb_2O_{5-x} for Aerobic Oxidation Through Synergy of Oxygen Vacancy and Porosity

Yuwei Wang[1], Fei Liu[1], Gareth R. Williams[2], Dongbin Zhang[1], Xianggui Kong[1,*], and Xiaodong Lei[1,*]

[1] State Key Laboratory of Chemical Resource Engineering, Beijing University of Chemical Technology, P.O. Box 98, Beijing 100029, China
[2] UCL School of Pharmacy, University College London, 29–39 Brunswick Square, London, WC1N 1AX, UK

A major reduction in energy consumption and the costs of catalysts will be required in future chemical manufacturing processes. To reach this goal, the transitional metal oxides (TMOs) as photocatalysts under solar energy have been widely studied. Nb_2O_5, as a promising photocatalyst, has attracted increasing attention owing to their unique properties. However, the intrinsic large bandgap of Nb_2O_5 hinder its potential applications in a variety of fields. Herein, we report an effective and simple strategy to synthesize black mesoporous Nb_2O_{5-x} nanorods (BMNb) with abundant oxygen vacancies. The formation of oxygen vacancy reduces the bandgap of Nb_2O_5 which extend the photoresponse from the ultraviolet to the visible and infrared light regions. In addition, The mesoporous structure of BMNb lead to a higher surface area than the as-prepared Nb_2O_5 precursor (36.24 m^2/g cf 8.69 m^2/g). Benefitting from coordinated regulation of structure and composition, the BMNb exhibits better photocatalytic performance than Nb_2O_5 in aerobic oxidative coupling of amines to imines under visible light irradiation at room temperature. The yield of BMNb for benzylamine oxidation increases by 63% over the Nb_2O_5. This work could open new perspectives to design TMOs with enhanced photocatalytic properties.

Keywords: Niobium Oxide, Particles, Photocatalyst, Microstructure, Aerobic Coupling.

1. INTRODUCTION

Transition metal oxides (such as TiO_2, ZnO, or Nb_2O_5) have been widely explored in various fields due to their their stability, abundance, accessibility, and environmental friendliness [1–3]. Nb_2O_5 as a typical *n*-type transition metal oxide semiconductor has been found to be potent in a range of applications, including acid catalysis, microelectronics, field emission displays, gas sensing, and electrochromics [4–8]. However, the intrinsic large bandgap of Nb_2O_5 (about 3.2 eV) restricts its potential applications in a variety of fields [9, 10]. Some studies reported that the introduction of oxygen vacancy in Nb_2O_5 could enhance light absorption in both the visible and near-infrared regions and facilitate charge separation and migration [11–13]. Nevertheless, the design of porous structure is usually ignored in previous Nb_2O_{5-x}, which vastly decreases the surface areas [14]. In fact, increasing the surface area is a potent approach to improve the catalytic efficiency [15–19]. Thus, it is necessary to develop an effective method to synthesize black mesoporous Nb_2O_{5-x} nanorods (BMNb) with enhaced photocatalytic performance.

As a classic organic reaction, aerobic coupling has been investigated deeply by many researchers [20, 21]. The reaction from amine to imine is significant industrially since the latter have a range of applications as intermediates in the chemical synthesis of biologically active and medicinal organic compounds [20]. Recently, the Zhang group employed the porous single-crystalline CdS nanosheets as efficient photocatalysts for aerobic oxidative coupling of amines to imines [22]. In addition, the Tanaka group used Nb_2O_5 as a photocatalyst for selective oxidation of benzylamine under visible light irradiation [23]. However, the Nb_2O_5 does not absorb the visible light. Thus, the search for transition metal oxide catalysts with efficient photocatalytic aerobic oxidative coupling of

*Authors to whom correspondence should be addressed.

amines to imines performance, especially under visible light irradiation, is rather desirable.

Herein we demonstrate an effective and simple strategy to synthesize black mesoporous Nb_2O_{5-x} nanorods (BMNb) with abundant oxygen vacancies. The formation of oxygen vacancy reduces the bandgap of Nb_2O_5 which extend the photoresponse from the ultraviolet to the visible and infrared light regions. In addition, The mesoporous structure of BMNb lead to a higher surface area than the as-prepared Nb_2O_5 precursor (36.24 m^2/g cf 8.69 m^2/g). Benefitting from synergy effect of structure and composition, the BMNb exhibits better photocatalytic performance than Nb_2O_5 in aerobic oxidative coupling of amines to imines under visible light irradiation at room temperature. The yield of BMNb for benzylamine oxidation increases by 63% over the Nb_2O_5.

2. EXPERIMENTAL DETAILS

The black mesoporous Nb_2O_{5-x} nanorods (BMNb) was synthesized as follows:

First, 0.26 g of Nb powder (99.8%) was dissolved in 40 mL of 10 M NaOH under stirring for 10 min. The resultant solution was transferred to a 50 mL Teflon-lined stainless steel autoclave and heated at 130 °C for 18 h. The solid products were recovered by vacuum filtration and rinsed with deionized water. This resulted in sodium niobate nanorods. These were next suspended in 100 mL of 2 M HCl for 24 h under stirring at room temperature to yield niobic acid rods. The protonated products were rinsed with deionized water repeatedly until the supernatant had a neutral pH before being dried at 80 °C overnight. The white Nb_2O_5 nanorods (WNb) were subsequently obtained after annealing at 700 °C in air for 3 h. To prepare mesoporous Nb_2O_5 nanorods (MNb), the WNb material was annealed at 700 °C for 3 h under a flow of ammonia in a tube furnace. The ammonia flow replaced with air for 2 h before the temperature was reduced to 550 °C. Finally, black mesoporous Nb_2O_{5-x} nanorods (BMNb) were obtained after annealing at 900 °C under a flow of 3% H_2/Ar. For comparison purposes, two control samples were also prepared. The first was generated by annealing WNb in air at 900 °C. Second, black Nb_2O_{5-x} nanorods (BNb) were obtained by H_2 reduction of WNb nanorods under a flow of 3% H_2/Ar at 900 °C.

X-ray diffraction (XRD) patterns were collected on a Rigaku UItima III instrument over the 2θ range between 3 and 70° at 10° min^{-1}. A Nicolet 380 instrument was used to obtain Fourier transform infrared (FTIR) spectra from 400–4000 cm^{-1}. Scanning electron microscopy (SEM) was conducted on a Zeiss Supra 55 microscope, while transmission electron microscopy (TEM) was undertaken with the aid of a JEOL JEM-2010 h-TEM (accelerating voltage: 200 kV). An ESCALAB 250 spectrometer (Thermo Scientific) equipped with a monochromatic 150 W Al Kα source was employed for X-ray photoelectron spectroscopy (XPS). The passing energy was 30 eV, and charge was compensated by low energy electrons. Binding energies are reported relative to the C 1*s* line at 284.8 eV. Diffuse reflectance ultraviolet and visible (DRUV-vis) spectroscopy was performed with a Tsushima UV-3600 UV-vis spectrometer over the wavelength range 200 to 1500 nm. Fine $BaSO_4$ powder was utilized as a standard material. Photoluminescence (PL) measurements were conducted using a CanyECLIPSe spectrophotometer (Varian). Nitrogen adsorption–desorption data were obtained with the aid of a Conta AS-1C-VP analyzer. All products were out-gassed at 373 K for 6 h, and the Brunauer–Emmett–Teller (BET) approach based on adsorption isotherms was employed to calculate the specific surface areas.

A double-neck flask (25 mL) was utilized to conduct photocatalytic reactions. An O_2 flow of 10 mL/min was established, and a 300 W xenon lamp (Beijing ChangTuo Ltd.) with a cut-off filter ($\lambda > 420$ nm) used as the light source. The distance between the light source and the center of the reaction solution was approximately 10 cm. The solution temperature was maintained at 30 °C. The initial benzylamine concentration and volume of acetonitrile (solvent) were 5 mmol and 10 mL, respectively. Before switching on the lamp, 100 mg of catalyst was added to this solution, and the resultant suspension stirred for 30 min in the dark to reach thermodynamic equilibrium. Quantitative analysis of the reaction products was performed on a GC-MS (Agilent 7890B-5977A, equipped with a DB-5MS capillary column). The reusability of the photocatalyst was determined using the same method but with repeated 5 h run times. After each experimental run, the photocatalyst was recovered using a centrifuge, washed with ethanol, and reused for the oxidation of fresh reactants.

The role played by hydroxyl radicals, superoxide radical species, and photogenerated holes in this photocatalytic system was determined in scavenging experiments. These were performed with the addition of 2 mL of isopropanol (IPA), 1 mM benzoquinone (BQ) or 1 mM ethylenediaminetetraacetic acid (EDTA). For all scavenging experiments, 100 mg of BMNb was added into 10 mL of a 5 mmol benzylamine in acetonitrile. Before switching on the lamp, the suspension was stirred for 30 min in the dark. Quantitative analysis of the reaction products was performed on a GC-MS (Agilent 7890B-5977A, equipped with a DB-5MS capillary column).

3. RESULTS AND DISCUSSION

XRD patterns of the various Nb_2O_5 materials are shown in Figure 1(a). The Bragg reflections of the white Nb_2O_5 nanorods (WNb) and mesoporous Nb_2O_5 nanorods (MNb) are consistent with the orthorhombic cell of Nb_2O_5 (T-Nb_2O_5, JCPDS No. 30-0873). However, after either an

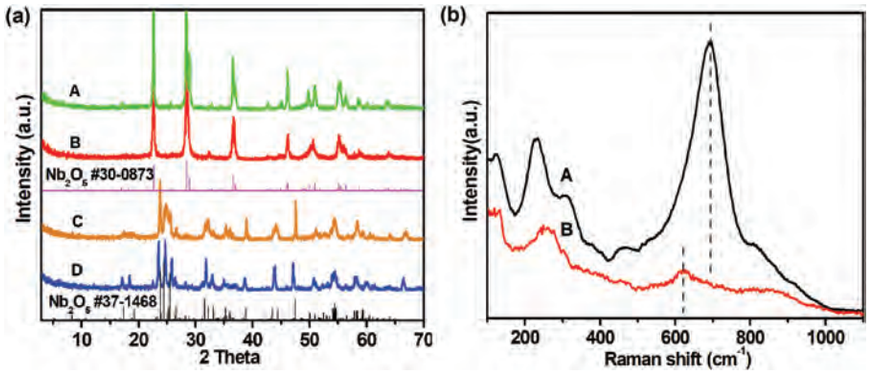

Figure 1. (a) XRD patterns of (A) white Nb_2O_5 (WNb), (B) white mesoporous Nb_2O_5 (MNb), (C) white mesoporous Nb_2O_5 obtained at 900 °C in air, and (D) black mesoporous Nb_2O_{5-x} obtained at 900 °C under H_2 (BMNb). (b) Raman spectra of (A) WNb, (B) BMNb.

air or H_2 annealing treatment at 900 °C, the XRD patterns are distinctly different and correspond to a monoclinic structure (Nb_2O_5, JCPDS No. 37-1468). While the XRD patterns of the black mesoporous Nb_2O_{5-x} nanorods (BMNb) and mesoporous Nb_2O_5 obtained at 900 °C in air are identical, a dramatic color change from white to black is observed after treatment under H_2. Overall, it is clear that BMNb has been synthesized successfully [24].

Raman spectroscopy was used to further investigate the structural changes occurring to the nanorods after H_2 treatment (Fig. 1(b)). Raman bands can be seen at 200–300 cm^{-1} for both the WNb and BMNb nanorods, but there is a distinct shift in position which is symptomatic of deformation modes and bridging of Nb–O–Nb bonds [25]. The broad band at around 700 cm^{-1} in the spectrum of the pristine WNb material fits well with the principal Nb–O stretching mode. In the case of the BMNb nanorods, the Nb–O stretching vibration has been broadened and moved to 620 cm^{-1}. These changes confirm that the original symmetry of the Nb_2O_5 lattice is reduced, as a result of the disordered surface introduced by the hydrogen annealing treatment [26].

The morphologies of pristine WNb and BMNb were studied by SEM and TEM (see Fig. 2). The samples comprise nanorods which are relatively uniform in terms of their sizes and aspect ratios. Both WNb (Figs. 2(a and b)) and BMNb (Figs. 2(c and d)) have similar morphologies, demonstrating that H_2 annealing does not change the morphology of the materials. Figure 2(e) depicts TEM images of the BMNb structures, and reveals that the rods are of around 100–150 nm in width with porous structures. The pores are around 10 nm diameter, and are distributed evenly through the nanorods. In contrast, the WNb nanorods have uniform solid structures (Fig. 2(f)). These observations are confirmed by BET analysis, which gives a surface area of 36.24 m^2/g for BMNb; this is threefold larger than the equivalent value for the WNb (8.69 m^2/g).

The composition and the surface electronic states of the materials were quantified by XPS analysis. Figure 3(a) gives the survey spectra of WNb and BMNb. All the peaks correspond to Nb, O and C, suggesting that there are no impurities in either material. In Figure 3(b), the detailed Nb 3*d* spectra are presented. The WNb sample has two obvious peaks (at 209.9 eV and 207.1 eV). These correspond to the $3d_{5/2}$ and $3d_{3/2}$ states of Nb^{5+}, with the positions agreeing well with the literature [27, 28]. In the spectrum of the BMNb sample, the $3d_{5/2}$ and $3d_{3/2}$ peaks have broadened, and are located at slightly lower values than the equivalent peaks of WNb. The difference in binding energies can be attributed to the existence of Nb^{4+} (207.6 eV) in the BMNb [29].

Previous studies have demonstrated that XPS can be a useful tool to indicate the existence of oxygen vacancies in transition metal oxides [30–32], and O 1*s* core level XPS spectra are presented in Figures 3(c)–(d). The O 1*s*

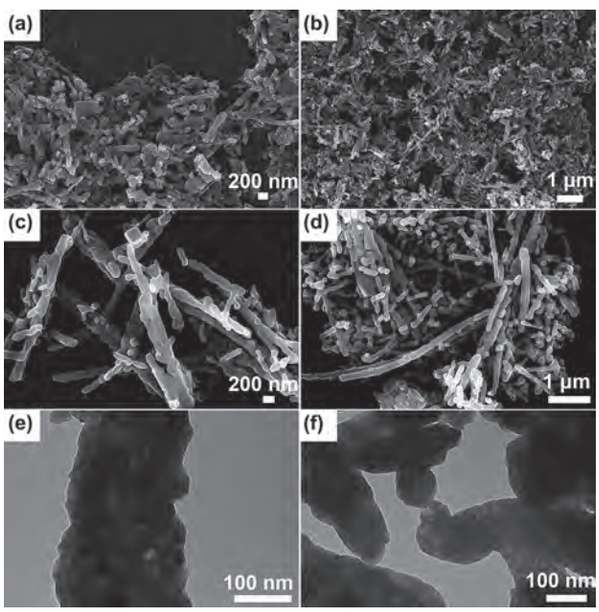

Figure 2. SEM images of the WNb (a, b) and BMNb nanorods (c, d), together with representative TEM images of the BMNb samples (e) and WNb samples (f).

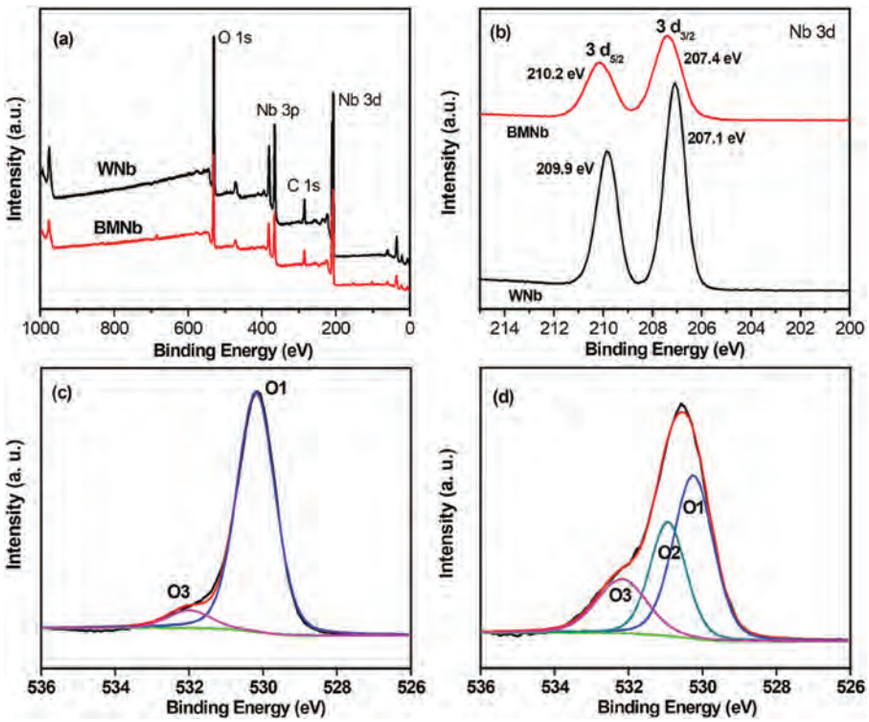

Figure 3. XPS spectra showing (a) a survey of WNb and BMNb, (b) the Nb 3*d* region, and the O 1*s* regions for (c) WNb and (d) BMNb. In (c) and (d), black lines correspond to the experimental spectra, and red lines the combined fit from all the O environments (O1: blue line; O2: cyan line; O3: magenta line).

spectrum of WNb in Figure 3(c) shows two typical peaks at O1 (530.2 eV) and O3 (532.1 eV). The O1 and O3 peaks can be ascribed to oxygen atoms bonded to metal and hydroxyl species of the surface-adsorbed water molecules [33, 34]. However, except the O1 and O3 peaks, there is O2 (531.1 eV) peak in O 1*s* spectrum of BMNb which is corresponding to oxygen defect sites with low oxygen coordination [35, 36]. Thus, these results further confirmed that oxygen vacancies are introduced into WMNb.

UV-visible diffuse reflectance spectroscopy (Fig. 4(a)) was used to examine the influence of oxygen vacancies on the bandgap energy of BMNb. The Kubelka-Munk equation was employed to calculate the bandgap of these materials (Fig. 4(a)) [37]. The optical absorption coefficient (α) is expected to vary with the photon energy (hv) in accordance with the relationship transition process. For a directly allowed transition, $n = 2$ [38]. The bandgap of WNb is approximately 3.09 eV, and its absorption edge is at ca. 400 nm. Compared to WNb, the absorption for

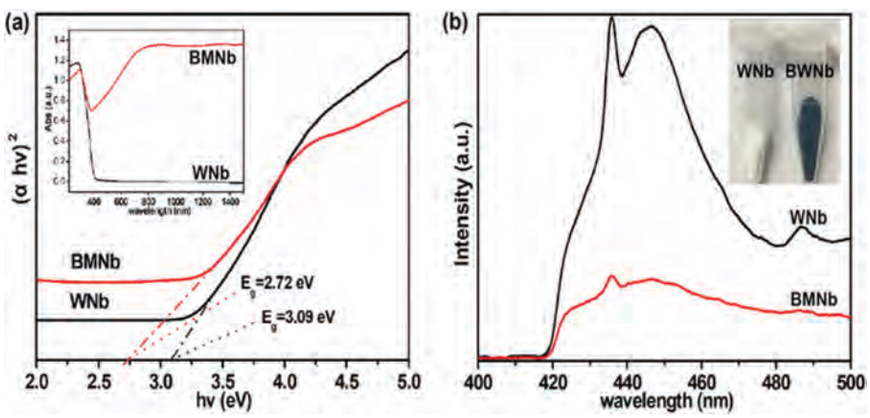

Figure 4. (a) Plots of $(\alpha hv)^2$ versus the energy of absorbed light for the WNb and BMNb nanorods (inset: Diffuse reflectance absorbance spectra). (b) Photoluminescence spectra of WNb (A) and BMNb (B) (inset: A photograph of the two samples).

BMNb shows a red shift, which represent a narrower bandgap (2.72 eV). It can be attributed to the formation of oxygen vacancies induced by H_2 annealing. The similar phenomenon has been reported in the studies of black TiO_2 [34]. Thus, the BMNb extends the photoresponse from UV light to the visible and near-infrared light regions due to the existence of oxygen vacancy.

Photoluminescence (PL) spectroscopy proves valuable insight on the behavior of semiconductors in terms of the efficiency of charge carrier trapping and recombination rate of electron–hole pairs. In general, PL emission arises from the recombination of free charge carriers, and the PL spectra of nanostructured materials are determined by the transfer of photo-induced electrons and holes [39]. The PL spectra of both the WNb and BMNb samples contain obvious exciton signals (see Fig. 4(b)), with both curves having similar shapes. No additional signals arise from the BMNb sample, but the intensity of PL emission has decreased and there is significant broadening. These observations arise because the emission bands in the sample mainly arise from the green band, which is correlated with the presence of oxygen vacancies [39]. The reduced excitonic intensities seen with BMNb demonstrate that the separation of photo-induced electrons and holes can be improved by the introduction of oxygen vacancies in BMNb (cf. WNb), and that the recombination of photogenerated electrons and holes is suppressed in BMNb [40, 41]. Electrons and holes recombine much more easily in WNb, as is clear from its greater relative PL emission intensity.

To understand the relationship between the presence of oxygen site defects and the photocatalytic activity of the materials, a comparative time dependent study of the ability of WNb, BNb (black Nb_2O_{5-x} nanorods) and BMNb to oxidize benzylamine to *N*-benzylidene benzylamine under visible light ($\lambda > 420$ nm) was performed. As shown in Figure 5(a), BMNb exhibits a more potent photocatalytic performance over 10 h than the other materials, with of *N*-benzylidene benzylamine obtained. This is an improvement of about 63% compared to WNb, and a 27% improvement over BNb. WNb still has some activity because, although it does not absorb visible light, direct electron excitation from a donor level associated with adsorbed amine does permit some oxidation [42, 43]. It is however very clear that after the introduce of oxygen vacancies in BMNb, the *N*-benzylidene benzylamine yield was greatly improved. To explore the effect of different parameters in the catalytic performance, we have conducted a series of control experiments. Firstly, we take the effect of crystal structure and oxygen vacancy into consideration. Because that the crystal structure varies with the introduction of oxygen vacancy, so we discuss their effect in catalytic performance together. So we

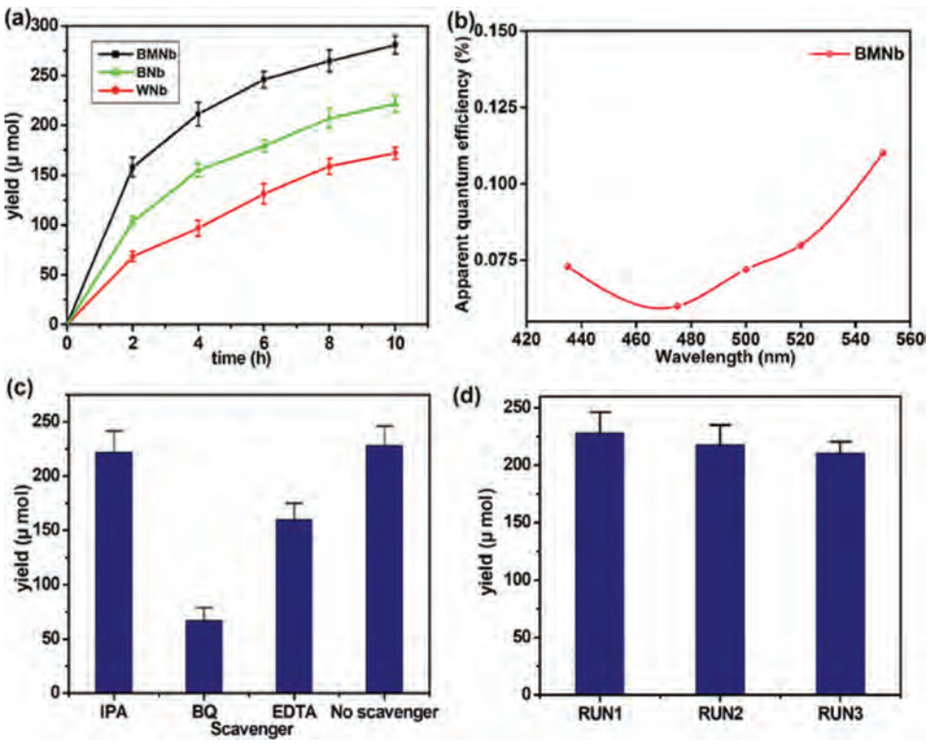

Figure 5. (a) The photocatalytic performance of WNb, BNb and BMNb in the oxidation of benzylamine to *N*-benzylidene benzylamine. (b) Apparent quantum efficiency (AQE) of BMNb under different wavelength light irradiation. (c) The results of a reactive species trapping experiment performed with BMNb under visible light. (d) The results of repeat cycling run in the photocatalytic oxidation of benzylamine over BMNb under visible light irradiation. All data are shown as mean ± S.D. from three independent experiments.

compare the catalytic performance of BNb and WNb normalised to surface area. The BNb (246.09 μmol/m^2, after 10 h) displayed better catalytic performance than WNb (198.10 μmol/m^2, after 10 h) normalised to surface area. So it can be concluded that the introduction of oxygen vacancy can improve the photocatalytic performance. Then is the effect of mesoporous structure. In this part, we compare the catalytic performance of BNb and BMNb as they have the same crystal structure and all have the presence of oxygen vacancy. BMNb (280.61 μmol, after 10 h) showed better catalytic performance than BNb (221.48 μmol, after 10 h). So it can be concluded that the mesoporous structure can also improve the photocatalytic performance.

To determine a photoexcited reaction, especially in a visible-light system, quantum efficiency is an essential factor. Herein, we calculate the apparent quantum efficiency (AQE) of the BMNb nanorods by measuring *N*-benzylidene benzylamine production amount at various wavelength of visible light under the same photoreaction conditions. As shown in Figure 5(b), the AQE was in agreement with the photoabsorption of BMNb nanorods. Under the above conditions, it can be found that the AQE was 0.11% at 550 nm.

To obtain further insight into the mechanism of the photocatalytic oxidative coupling, three additional experiments were performed (Fig. 5(c)). Three different scavenger species were explored: isopropanol (IPA, a scavenger for hydroxyl radicals), benzoquinone (BQ, for superoxide radical species), and ethylenediaminetetraacetic acid (EDTA, for photogenerated holes) were added to the catalytic experiment. The addition of BQ had a profound influence on the process, significantly lowering the yield of imine. This shows that the presence of superoxide radical species has a highly positive influence on the catalytic process. Similarly, the addition of EDTA also had a negative effect on the yield of the catalytic process, in agreement with previous results and confirming that holes generated are also of importance [42, 43]. However, there is no visible change in the yield with the addition of IPA, demonstrating that $^{\cdot}$OH radicals do not play a major role in the catalytic process.

Based on the above results, a mechanism for the oxidation of primary amines to imines in the presence of BMNb can be proposed (Fig. 6). The introduction of oxygen vacancies in BMNb narrowed the band gap and made the absorption edge shifted into the visible light and near-infrared region, thus improving its performance under visible light irradiation. When BMNb is exposed to light, O_2 molecules accept an additional electron generated by semiconductor photoexcitation. This results in the presence of $O_2^{\cdot-}$ radicals. Simultaneously, the primary amine is transferred to a cationic radical intermediate through loss of an electron. The holes (h^+) in the semiconductor will capture the latter. The cationic intermediate can then lose both a proton and neighboring hydrogen atom to the superoxide radical anion ($O_2^{\cdot-}$), which generates Ph–CH = NH.

It is well known that there are two different oxidation-dehydrogenation routes for oxidizing primary amines, which both involve the formation of a R–CH = NH intermediate [44]. In the first route, a second molecule of the primary amine attacks this intermediate to generate a second intermediate Ph–CH_2–NH–CH(NH_2)–Ph. This will then convert to an aminal, which will lose NH_3 via the hole-assisted elimination of an amine species, thus yielding the coupled imine product RCH = NCH_2R. In the second route, an aldehyde RCH = O will be generated through reaction between the initially formed imine and trace amounts of H_2O, but this will soon react with a second molecule of the amine to give the imine product. In the Nb_2O_5-photocatalyzed reaction system described here, no benzaldehyde was detected by GC. Therefore, it is more likely that The BMNb-catalyzed amine oxidation took the first route.

The recyclability of photocatalysts is crucial for industrial applications. A recycling experiment was hence conducted for the oxidation of benzylamine using BMNb (reaction time: 5 h). After three cycles, the BMNb photocatalyst still has good stability and recyclability, as

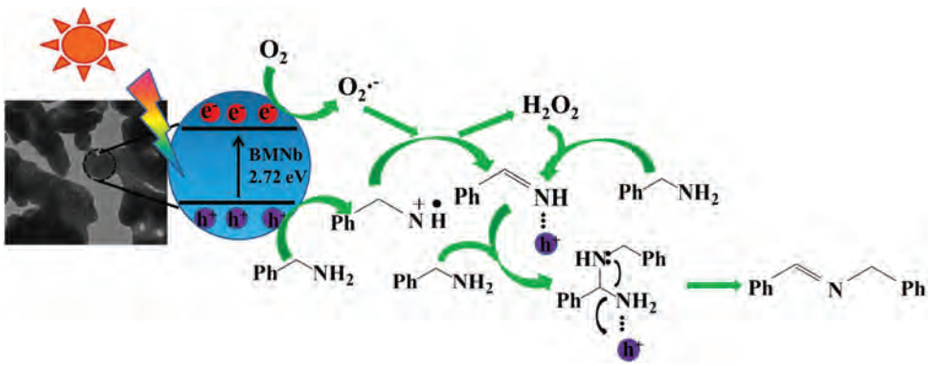

Figure 6. The proposed mechanism underlying the BMNb-catalyzed aerobic oxidative coupling of benzylamine to imines under visible-light irradiation.

demonstrated by the data in Figure 5(d). It is hence clear that BMNb is a promising photocatalyst for the aerobic oxidative coupling of amines under sunlight, especially since it maintains a high level of activity after recycling.

4. CONCLUSION

In conclusion, we report in this work a facile synthesis route to obtain mesoporous black Nb_2O_{5-x} (BMNb) nanorods. The formation of oxygen vacancy reduces the bandgap of Nb_2O_5 which extend the photoresponse from the ultraviolet to the visible and infrared light regions. In addition, The mesoporous structure of BMNb lead to a higher surface area than the as-prepared Nb_2O_5 precursor (36.24 m^2/g cf 8.69 m^2/g). Benefitting from synergy effect of oxygen vacancy and porous structure, the BMNb displays a promising application in aerobic oxidative coupling of benzylamine to *N*-benzylidene benzylamine, where BMNb gave a yield 63% greater than solid defect-free Nb_2O_5 nanorods of similar size.

Acknowledgments: This work was supported by the 973 Program (No. 2014CB932104), the National Natural Science Foundation of China (Nos: 2177060378 and U1707603) and the Program for Changjiang Scholars, Innovative Research Team in University (No. IRT1205).

References and Notes

1. Zahran, E.M., Bedford, N.M., Nguyen, M.A., Chang, Y.J., Guiton, B.S., Naik, R.R., Bachas, L.G. and Knecht, M.R., **2014**. Light-activated tandem catalysis driven by multicomponent nanomaterials. *Journal of the American Chemical Society*, *136*(1), pp.32–35.
2. Christopher, P., Xin, H., Marimuthu, A. and Linic, S., **2012**. Singular characteristics and unique chemical bond activation mechanisms of photocatalytic reactions on plasmonic nanostructures. *Nature Materials*, *11*(12), pp.1044–1050.
3. Linic, S., Aslam, U., Boerigter, C. and Morabito, M., **2015**. Photochemical transformations on plasmonic metal nanoparticles. *Nature Materials*, *14*(6), pp.567–576.
4. Wang, Y.D., Yang, L.F., Zhou, Z.L., Li, Y.F. and Wu, X.H., **2001**. Effects of calcining temperature on lattice constants and gas-sensing properties of Nb_2O_5. *Materials Letters*, *49*(5), pp.277–281.
5. Carniti, P., Gervasini, A. and Marzo, M., **2008**. Dispersed NbO_x catalytic phases in silica matrixes: Influence of niobium concentration and preparative route. *The Journal of Physical Chemistry C*, *112*(36), pp.14064–14074.
6. Mujawar, S.H., Inamdar, A.I., Patil, S.B. and Patil, P.S., **2006**. Electrochromic properties of spray-deposited niobium oxide thin films. *Solid State Ionics*, *177*(37), pp.3333–3338.
7. Jose, R., Thavasi, V. and Ramakrishna, S., **2009**. Metal oxides for dye-sensitized solar cells. *Journal of the American Ceramic Society*, *92*(2), pp.289–301.
8. Ahn, K.S., Kang, M.S., Lee, J.K., Shin, B.C. and Lee, J.W., **2006**. Enhanced electron diffusion length of mesoporous TiO_2 film by using Nb_2O_5 energy barrier for dye-sensitized solar cells. *Applied Physics Letters*, *89*(1), pp.013103–013108.
9. Rani, R.A., Zoolfakar, A.S., O'Mullane, A.P., Austin, M.W. and Kalantar-Zadeh, K., **2014**. Thin films and nanostructures of niobium pentoxide: Fundamental properties, synthesis methods and applications. *Journal of Materials Chemistry A*, *2*(38), pp.15683–15703.
10. Zuo, F., Wang, L., Wu, T., Zhang, Z., Borchardt, D. and Feng, P., **2010**. Self-doped Ti^{3+} enhanced photocatalyst for hydrogen production under visible light. *Journal of the American Chemical Society*, *132*(34), pp.11856–11857.
11. Gordon, T.R., Cargnello, M., Paik, T., Mangolini, F., Weber, R.T., Fornasiero, P. and Murray, C.B., **2012**. Nonaqueous synthesis of TiO_2 nanocrystals using TiF_4 to engineer morphology, oxygen vacancy concentration, and photocatalytic activity. *Journal of the American Chemical Society*, *134*(15), pp.6751–6761.
12. Cheng, H., Kamegawa, T., Mori, K. and Yamashita, H., **2014**. Surfactant-free nonaqueous synthesis of plasmonic molybdenum oxide nanosheets with enhanced catalytic activity for hydrogen generation from ammonia borane under visible light. *Angewandte Chemie*, *126*(11), pp.2954–2958.
13. Tada, H., Mitsui, T., Kiyonaga, T., Akita, T. and Tanaka, K., **2006**. All-solid-state Z-scheme in CdS–Au–TiO_2 three-component nanojunction system. *Nature Materials*, *5*(10), pp.782–786.
14. Zhao, W., Zhao, W., Zhu, G., Lin, T., Xu, F. and Huang, F., **2016**. Black Nb_2O_5 nanorods with improved solar absorption and enhanced photocatalytic activity. *Dalton Transactions*, *45*(9), pp.3888–3894.
15. Li, S., Schmidt, C.N., Xu, Q., Cao, X. and Cao, G., **2016**. Macroporous nanostructured Nb_2O_5 with surface Nb^{4+} for enhanced lithium ion storage properties. *ChemNanoMat*, *2*(7), pp.675–680.
16. Wang, L., Bi, X. and Yang, S., **2016**. Partially single-crystalline mesoporous Nb_2O_5 nanosheets in between graphene for ultrafast sodium storage. *Advanced Materials*, *28*(35), pp.7672–7679.
17. Chen, X., Yu, T., Fan, X., Zhang, H., Li, Z., Ye, J. and Zou, Z., **2007**. Enhanced activity of mesoporous Nb_2O_5 for photocatalytic hydrogen production. *Applied Surface Science*, *253*(20), pp.8500–8506.
18. Kondo, J.N., Uchida, M., Nakajima, K., Daling, L., Hara, M. and Domen, K., **2004**. Synthesis, mesostructure, and photocatalysis of a highly ordered and thermally stable mesoporous Mg and Ta mixed oxide. *Chemistry of Materials*, *16*(22), pp.4304–4310.
19. Li, Y., Fu, Z.Y. and Su, B.L., **2012**. Hierarchically structured porous materials for energy conversion and storage. *Advanced Functional Materials*, *22*(22), pp.4634–4667.
20. Murahashi, S.I., **1995**. Synthetic aspects of metal-catalyzed oxidations of amines and related reactions. *Angewandte Chemie International Edition in English*, *34*(22), pp.2443–2465.
21. Punniyamurthy, T., Velusamy, S. and Iqbal, J., **2005**. Recent advances in transition metal catalyzed oxidation of organic substrates with molecular oxygen. *Chemical Reviews*, *105*(6), pp.2329–2364.
22. Zhao, W., Liu, C., Cao, L., Yin, X., Xu, H. and Zhang, B., **2013**. Porous single-crystalline CdS nanosheets as efficient visible light catalysts for aerobic oxidative coupling of amines to imines. *RSC Advances*, *3*(45), pp.22944–22948.
23. Furukawa, S., Ohno, Y., Shishido, T., Teramura, K. and Tanaka, T., **2011**. Selective amine oxidation using Nb_2O_5 photocatalyst and O_2. *ACS Catalysis*, *1*(10), pp.1150–1153.
24. Graça, M.P. F., Meireles, A., Nico, C. and Valente, M.A., **2013**. Nb_2O_5 nanosize powders prepared by sol–gel-Structure, morphology and dielectric properties. *Journal of Alloys and Compounds*, *553*, pp.177–182.
25. Chen, X., Liu, L., Liu, Z., Marcus, M.A., Wang, W.C., Oyler, N.A., Grass, M.E., Mao, B., Glans, P.A. and Peter, Y.Y., **2013**. Properties of disorder-engineered black titanium dioxide nanoparticles through hydrogenation. *Scientific Reports*, *3*, pp.1510–1516.
26. Zhou, W., Li, W., Wang, J.Q., Qu, Y., Yang, Y., Xie, Y., Zhang, K., Wang, L., Fu, H. and Zhao, D., **2014**. Ordered mesoporous black TiO_2 as highly efficient hydrogen evolution photocatalyst. *Journal of the American Chemical Society*, *136*(26), pp.9280–9283.
27. Li, G.R., Hu, T., Pan, G.L., Yan, T.Y., Gao, X.P. and Zhu, H.Y., **2008**. Morphology-function relationship of ZnO: polar planes, oxygen vacancies, and activity. *The Journal of Physical Chemistry C*, *112*(31), pp.11859–11864.

28. Ge, S., Jia, H., Zhao, H., Zheng, Z. and Zhang, L., **2010**. First observation of visible light photocatalytic activity of carbon modified Nb_2O_5 nanostructures. *Journal of Materials Chemistry*, *20*(15), pp.3052–3058.

29. Liu, F., Cheng, X., Xu, R., Wu, Y., Jiang, Y. and Yu, Y., **2018**. Binding sulfur-doped Nb_2O_5 hollow nanospheres on sulfur-doped graphene networks for highly reversible sodium storage. *Advanced Functional Materials*, *28*(18), p.1800394.

30. Furukawa, S., Shishido, T., Teramura, K. and Tanaka, T., **2012**. Photocatalytic oxidation of alcohols over TiO_2 covered with Nb_2O_5. *ACS Catalysis*, *2*(1), pp.175–179.

31. Khan, M.M., Ansari, S.A., Amal, M.I., Lee, J. and Cho, M.H., **2013**. Highly visible light active Ag@TiO_2 nanocomposites synthesized using an electrochemically active biofilm: A novel biogenic approach. *Nanoscale*, *5*(10), pp.4427–4435.

32. Sun, Y., Liu, Q., Gao, S., Cheng, H., Lei, F., Sun, Z., Jiang, Y., Su, H., Wei, S. and Xie, Y., **2013**. Pits confined in ultrathin cerium (IV) oxide for studying catalytic centers in carbon monoxide oxidation. *Nature Communications*, *4*, p.2899.

33. Bao, J., Zhang, X., Fan, B., Zhang, J., Zhou, M., Yang, W., Hu, X., Wang, H., Pan, B. and Xie, Y., **2015**. Ultrathin spinel-structured nanosheets rich in oxygen deficiencies for enhanced electrocatalytic water oxidation. *Angewandte Chemie International Edition*, *54*(25), pp.7399–7404.

34. Zhu, C., Fu, S., Du, D. and Lin, Y., **2016**. Facilely tuning porous $NiCo_2O_4$ nanosheets with metal valence-state alteration and abundant oxygen vacancies as robust electrocatalysts towards water splitting. *Chemistry—A European Journal*, *22*(12), pp.4000–4007.

35. Gao, S., Jiao, X., Sun, Z., Zhang, W., Sun, Y., Wang, C., Hu, Q., Zu, X., Yang, F. and Yang, S., **2016**. Ultrathin Co_3O_4 layers realizing optimized CO_2 electroreduction to formate. *Angewandte Chemie International Edition*, *55*(2), pp.698–702.

36. Cheng, F., Zhang, T., Zhang, Y., Du, J., Han, X. and Chen, J., **2013**. Enhancing electrocatalytic oxygen reduction on MnO_2 with vacancies. *Angewandte Chemie*, *125*(9), pp.2534–2537.

37. Song, F., Schenk, K. and Hu, X., **2016**. A nanoporous oxygen evolution catalyst synthesized by selective electrochemical etching of perovskite hydroxide $CoSn(OH)_6$ nanocubes. *Energy & Environmental Science*, *9*(2), pp.473–477.

38. Ansari, S.A., Khan, M.M., Kalathil, S., Nisar, A., Lee, J. and Cho, M.H., **2013**. Oxygen vacancy induced band gap narrowing of ZnO nanostructures by an electrochemically active biofilm. *Nanoscale*, *5*(19), pp.9238–9246.

39. Lv, J., Li, C. and BelBruno, J., **2013**. Defect evolution on the optical properties of H^+-implanted ZnO whiskers. *CrystEngComm*, *15*(28), pp.5620–5625.

40. Liqiang, J., Yichun, Q., Baiqi, W., Shudan, L., Baojiang, J., Libin, Y., Wei, F., Honggang, F. and Jiazhong, S., **2006**. Review of photoluminescence performance of nano-sized semiconductor materials and its relationships with photocatalytic activity. *Solar Energy Materials and Solar Cells*, *90*(12), pp.1773–1787.

41. Shishido, T., Miyatake, T., Teramura, K., Hitomi, Y., Yamashita, H. and Tanaka, T., **2009**. Mechanism of photooxidation of alcohol over Nb_2O_5. *The Journal of Physical Chemistry C*, *113*(43), pp.18713–18718.

42. Zhang, H., Wu, Q., Guo, C., Wu, Y. and Wu, T., **2017**. Photocatalytic selective oxidation of 5-hydroxymethylfurfural to 2, 5-diformylfuran over Nb_2O_5 under visible light. *ACS Sustainable Chemistry & Engineering*, *5*(4), pp.3517–3523.

43. Su, F., Mathew, S.C., Möhlmann, L., Antonietti, M., Wang, X. and Blechert, S., **2011**. Aerobic oxidative coupling of amines by carbon nitride photocatalysis with visible light. *Angewandte Chemie*, *123*(3), pp.683–686.

44. Lang, X., Ji, H., Chen, C., Ma, W. and Zhao, J., **2011**. Selective formation of imines by aerobic photocatalytic oxidation of amines on TiO_2. *Angewandte Chemie International Edition*, *50*(17), pp.3934–3937.

Received: 3 September 2018. Accepted: 1 April 2019.